ISCST
2012

NANOMATERIALS AND NANOSCALE COATINGS

Convective Assembly for Nanostructured Optical and Biofunctional Coatings

A. Weldon, T. Muangnapoh, P. Kumnorkaew, and J. F. Gilchrist(*)

(*) Department of Chemical Engineering
Lehigh University, Bethlehem, Pennsylvania 18015

Presented at the 16th International Coating Science and Technology Symposium,
September 9-12, 2012, Midtown Atlanta, GA[1]

There is perhaps no simpler way of modifying surface chemistry and morphology than surface deposition of particles. To this effect, we are developing a process where nanoscale and micron-sized microspheres are deposited onto surfaces. The process is drawing a thin films of suspension and driving self-organization via rapid convective deposition. This process is similar to the `coffee ring effect' using a similar method to that studied by Prevo and Velev, (*Langmuir*, 2003). In our studies, we alter the interactions between particles by controlling the thin film profile by varying deposition rate, substrate motion, blade angle, and blade chemistry to optimize the operating conditions where 2D close-packed arrays of microspheres existed. Self-assembly of colloidal particles through a balance of electrostatic and capillary forces during solvent evaporation drive this assembly within the thin film. These interactions were explored through a model comparing the residence time of a particle in the thin film and the characteristic time of capillary-driven crystallization to describe the morphology and microstructure of deposited particles. Co-deposition of binary suspensions of micron and nanoscale particles was tailored to generate higher-quality surface coatings and a simple theory describes the immergence of instabilities that result in formation of stripes.

Beyond the intriguing fundamental science behind the deposition process is a multitude of functional materials made possible using this deposition process. Microspheres partially buried in codeposited polymer can act as microlens arrays. Coated atop LEDs, a drastic increase in device performance results from the enhanced photon extraction efficiency of these structures. Similarly, these structures can be incorporated into dye sensitized solar cells and this process can also be used to engineer dye supports that enhance device performance. Likewise, these coatings can make physically and chemically heterogeneous surfaces that can be optimized for targeted cell capture for disease detection. In one example, tuning the surface roughness is shown to nontrivially alter capture of CD4+ lymphocytes suggesting a coupling between the periodicity of the surface and the selective capture mechanisms of these infected cells for HIV detection. This deposition process is now being expanded into a scalable nanomanufacturing process where roll-to-roll coatings are made possible for commercial applications.

---

[1] Unpublished. ISCST shall not be responsible for statements or opinions contained in papers or printed in its publications.

ULTRATHIN COATINGS OF EXFOLIATED ZEOLITE NANOSHEETS ON POROUS AND NON-POROUS SUPPORTS

Kumar V. Agrawal, Lorraine. F. Francis, Michael Tsapatsis

Department of Chemical Engineering & Material Science
The University of Minnesota, Minneapolis, Minnesota 55455

Sustainable technologies are needed to replace energy inefficient separation processes, such as distillation and crystallization. Distillation alone is responsible for nearly 40% of total consumed energy in the chemical industry. Separation using membranes is a promising, energy efficient alternative. Zeolites are especially attractive as membrane materials. These aluminosilicates have well-defined cages and channels built into the crystal structure as well as high chemical and thermal stability. The size range of the cages and channels in the zeolite structure is 3-20 Å, similar to the sizes of many industrially important molecules. Therefore, membranes fabricated using zeolites can selectively sieve various gases and hydrocarbon vapors. Further, thin zeolite films made using exfoliated zeolite nanosheets have the potential for outstanding performance by creating a combination of high flux and selectively.

Here we report exfoliation of zeolite nanosheets from their layered as-grown zeolite precursor and subsequent coating of these nanosheets on porous and non-porous supports using filtration and evaporation assisted self assembly. Exfoliation of nanosheets by a melt shearing process was confirmed by transmission electron microscopy and X-ray diffraction. Scanning probe microscopy indicated that zeolite nanosheets were 1.5 unit cell (~ 3.4 nm) thick along their *b*-axis. The coating morphology, characterized by scanning electron microscopy, revealed that a

---

coating prepared by filtration on a porous support consisted of well packed, overlapping nanosheets (Figure 1). Films made on porous supports separated equimolar feed of *p*-xylene and *o*-xylene with the separation factor of 40-70 after a very mild hydrothermal treatment (Varoon *et al.,* 2011).
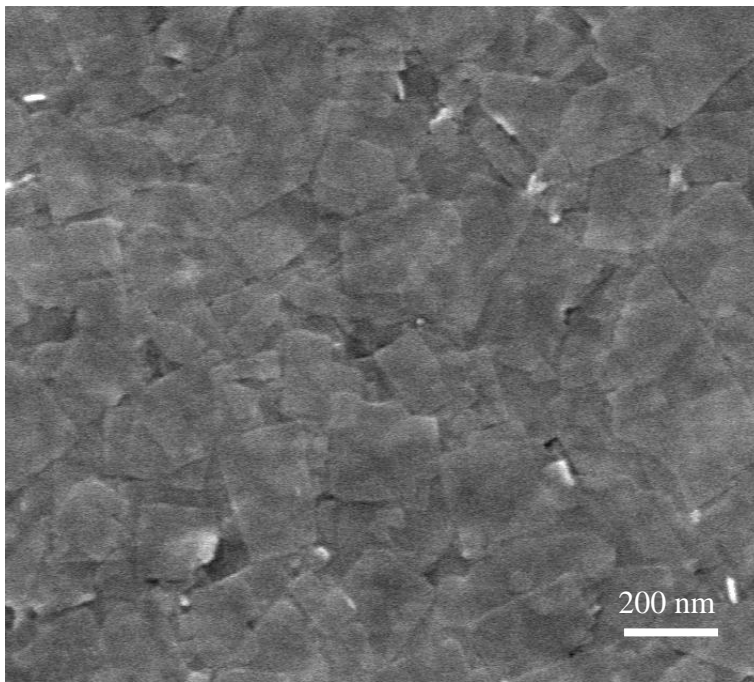

Figure 1: SEM of zeolite nanosheet coating with b-axis orientation on a porous support

Reference:

K. Varoon, X. Zhang, B. Elyassi, D. D. Brewer, M. Gettel, S. Kumar, J. A. Lee, S. Maheshwari, A. Mittal, C. Y. Sung, M. Cococcioni, L. F. Francis, A. V. McCormick, K. A. Mkhoyan, M. Tsapatsis, "Dispersible Exfoliated Zeolite Nanosheets and Their Application as a Selective Membrane", **Science**, 334, 72, 2011

Nanostructure and electrical properties of organic semiconductor thin films prepared by wet and dry processing:

Yoshiko TSUJI[1, 2 *] and Yukio YAMAGUCHI[2]

[1] Environmental Science Center, The University of Tokyo

Hongo 7-3-1, Bunkyo-ku, Tokyo, 113-0033, Japan

[2] Department of Chemical System Engineering, The University of Tokyo

Hongo 7-3-1, Bunkyo-ku, Tokyo, 113-8656, Japan

1. Introduction

Solution processed electronic devices such as low molecule OLEDs are now attracting research interests because of the benefits of cost-effective mass production. To improve electric/optical properties, it is necessary to control the nanostructure of thin films on a macroscale. We have already reported that the solvent influences crystal growth kinetics and crystal structures of polycrystalline organic semiconductor thin films in solution process [1]. In this work, we focus on amorphous organic semiconductor films and investigate the effect of dry/wet processes on the characteristics.

2. Experimental details

In this study, we use three types of precursors, where they have different crystallinity, solubility for toluene, and melting point as shown in table 1. Evaporation coating was performed for these organics (PVD process). Solution process of spin coating was also performed. Single crystal and precipitated powder were

---

[1] Unpublished. ISCST shall not be responsible for statements or opinions contained in papers or printed in its publications.

obtained by drying up solution.

Table 1. Low molecule organic materials in this study.

material	csyatallinity	solubility
A	crystal	~1.5
B	amorphous	~13
C	amorphous	~40

The characterizations of structures were performed by 2θ X-ray diffraction (XRD) with Cu Kα radiation operating at 50 kV and 300 mA on an X-ray diffractometer (Rigaku, ATX-G), transmission electron microscopy (TEM; JEOL, JEM-4010) operating at 400 kV or 200 kV, electron diffraction, and Fourier transform infrared spectroscopy (FTIR; Perkin-Elmer, Spectrum One). Thermo analysis was also performed by a Thermogravimetry-Differential Thermal Analysis and Mass Spectrometry (TG-DTA-MS; Rigaku, Thermo plus) to identify the residual solvent in precipitated powder and scraped powder from spin coated films on Si substrates. Optical properties were measured by UV-vis spectrometer (Hitachi, U-4100) and photoluminescence.

3. Results and discussions

3-1. PVD films

Figure 1 shows typical XRD patterns of PVD films deposited below the crystallization temperature. The films had amorphous structure and each XRD pattern showed a halo peak around 20°. The d-spacing corresponding to the intermolecular distance was determined from the halo peak. Despites the substrate temperature, it took constant value based on each
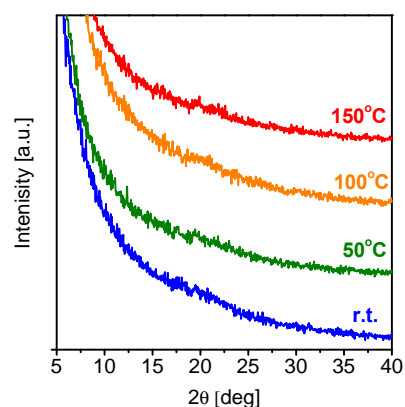

FIG. 1. XRD spectra of PVD films

organic material. Optical energy gap was obtained from absorption edge wavelength, and it also took the constant value based on each organic material.

3-2. Spin coated films

From XRD and TEM observation, spin coated films were confirmed to have amorphous structure independent of spin rate. D-spacing between molecules and optical energy gap of spin coated films was determined and it was found that spin rate affected the properties of the films. A higher spin rate, which corresponds to a higher drying rate, results in a smaller d-spacing value and a smaller optical energy gap. By focusing on the relationship between d-spacing and optical energy gap as shown in Fig. 2, it is obvious that the

FIG. 2. Relationship between d-spacing and optical energy gap of spin coated films.

energy gap decreases with the decrease of d-spacing probably due to the development of π-π conjugation.

To understand the effect of solvent, we determined the precipitated powder from toluene and THF solution, by drying up with different rate. The precipitated powder has amorphous structure when dried up fast, and has polycrystalline structure when dried up slowly. In the thermal analysis of precipitated powder, a three-step weight loss was observed due to solvent molecule. With increasing drying rate, the desorption of solvent corresponding to the second peak decreased, and the one corresponding to the third peak increased. We consider that precipitated powder contains solvent with three different modes, the first one caused by the solution from powder surface, the second one caused by the solvent adsorbed with molecules on the domain boundaries, and the third one, which is desorbed at melting point, caused by the solvent adsorbed much stronger than the second one with molecules in the domains.

We observed a phase transition from a toluene solution to a solid thin film during spin coating process using in-situ measurements of the PL spectra and the variation of scattered light [2]. As shown in Fig. 3, the gradual decrease in PL intensity was observed from 0 to $\tau 1$ due to the formation of a solid-like surface. The sudden increase in PL intensity was observed between $\tau 1$ and $\tau 2$, and the variation of the scattered light intensity that represented the fluctuation of the top surface suddenly decreased at $\tau 2$. We consider that $\tau 1$
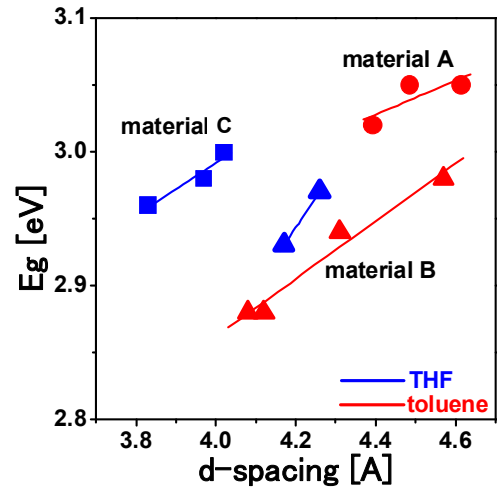
corresponds to the onset of the formation of the solid film, which should be a critical super-saturation point on the solubility curve, and the phase transition of the solute to the solid is completed at $\tau 2$.
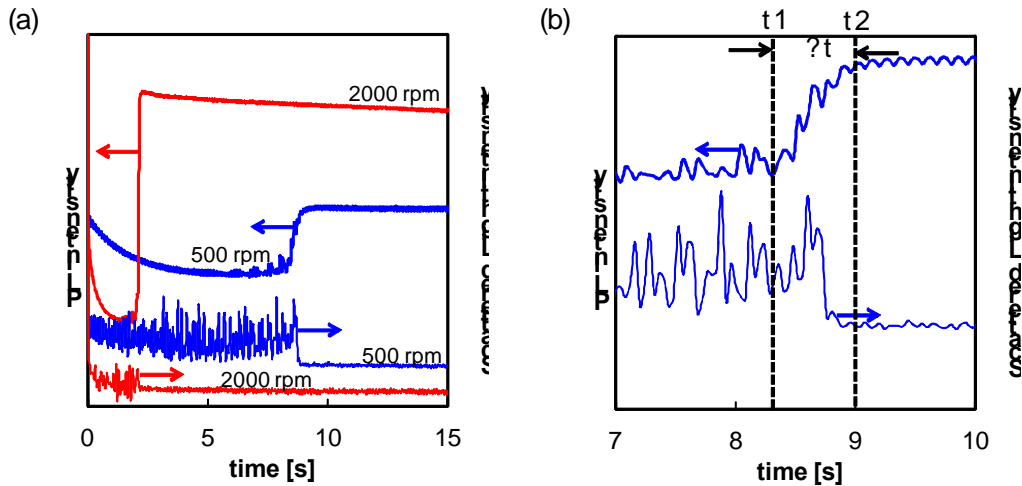

FIG. 3. In situ measurements of PL and scattered light during spin coating. (b) shows the magnified spectra between τ1 and τ2.

Basically when the drying rate is fast, the solution concentration at critical super-saturation point is higher, causing the higher nucleation frequency, so that the domain size would be small. When the domain size is small, the diffusion length of residual solvent decreases and it becomes easy to diffuse solvent outside to the atmosphere, and introduces the small amount of residual solvent in the domains. And then, d-spacing tends to small, results in small optical energy gap.

4. Conclusions

We focused on the amorphous low molecular organic semiconductor films, and clarified the relationship among "process" including wet process and evaporation process, "structure" (d-spacing between molecules), and "property" (optical band gap or photoluminescence property). Though d-spacing and Eg were independent of process parameters in PVD films, they strongly depend on process parameter in spin coated films. The structure of the film is estimated by considering the dynamics of film formation, and the optical property is determined by d-spacing between molecules.

References: [1] Y. Tsuji, K. Uehara, E. Narita, A. Ono, N. Mizuno, and Y. Yamaguchi, Pacifichem 2010, Honolulu, Hawaii, USA, Dec. 17th-20th, 2010. [2] K. Oku, S. Inasawa, Y. Tsuji, and Y. Yamaguchi, Dry. Technol., 30 (8), 832-838 (2012).

Improving Surface Properties by Laser-based Drying, Gelation and Densification of Printed Sol-Gel Coatings

D. Hawelka*, J. Stollenwerk**, N. Pirch*, K. Wissenbach*

* Fraunhofer Institute for Laser Technology (ILT)
Steinbachstraße 15, 52074 Aachen, Germany

** Chair for the Technology of Optical Systems (TOS)
RWTH Aachen University, Steinbachstraße 15, 52074 Aachen, Germany

Introduction

Functional coatings are a powerful tool to improve properties and to widen the application range of various components. For this purpose industry highly demands low-cost and resource efficient coating processes that are easy to integrate into production lines. Wear protection coatings are required to increase the lifetime of highly-stressed mechanical components in many industrial sectors (e.g. automobile, alternative energy). In many cases, conventional expensive batch-based vacuum processes (e.g. PVD) are not applicable due to the required high throughput or huge dimensions of the components. Therefore inline-capable wet-chemical coating processes hold great potential to become an alternative. Major challenges of these innovative technologies are the application of the liquid coating material and the thermal post-treatment required for the transformation into a dried and densified layer with the desired properties. The developed inline coating process for the production of highly wear resistant coatings consists of three steps. In the first step a zirconia-based sol-gel coating material is applied to hardened steel substrates by a wet-chemical coating process (e.g. pipe-jet printing, spin-coating). In the second step a laser process is used to dry the wet thin film and remove the organic ingredients. Finally, a second laser process is used to generate adapted temperature-time-profiles in order to achieve peak temperatures > 1200 °C required for the functionalization of the films without reducing the hardness of the hardened steel substrate having a low thermal stability of 180 °C.

Experimental

Within previous investigations carried out in close collaboration with Merck KGaA Darmstadt, Schaeffler KG, Dilas GmbH and Biofluidix GmbH sol-gel coating applied by spin-coating have been dried and functionalized by a two-stage laser process [1, 2]. Organic ingredients were removed by the first laser treatment carried out with continuous diode laser radiation. Within the second laser treatment carried out with pulsed diode laser radiation it was possible to increase the coating hardness to more than 1000 HV. The investigations presented in this paper focus on the application of an inline-capable printing process in order to substitute the spin-coating process

---

and on the laser-based drying of these printed coatings. The Biofluidix Biospot 600 device is used to print drops of the coating material with a diameter of (5± 0,5) mm onto the steel surface cleaned with alcohol. The drops are deposited in a honeycomp structure with a pitch of 3 mm in order to achieve a uniform and homogeneous thin film. The printed green films still contain solvents and uncondensed molecular precursors. Applying very high temperatures to the undried sol-gel coating (green film) leads to the decomposition of the applied green film. Therefore, the following aspects must be considered:

1. Solvents need to be removed (drying).
2. A high degree of network formation needs to be achieved (gelation) without exceeding the decomposition temperature of the molecular precursors.
3. Due to the single-layer thickness of ≤ 100 nm, multilayer systems with a thickness of ≥ 400 nm must be generated to enable an accurate measurement of the mechanical properties without any influence of the substrate.

The aim of the investigation presented in this paper is to develop a laser-based process to handle these tasks. Continuous diode laser radiation (wavelength $\lambda = 980$ nm) is used to generate temperatures < 800 °C. In order to achieve a two-dimensional treatment a 2D galvano scanner is used to guide the laser-spot across the coated surface in a meander-shaped track (Figure 1). The resulting laser process parameters are: laser output power P_L, beam diameter d_S, hatch spacing d_y, scanning velocity v_{scan}.
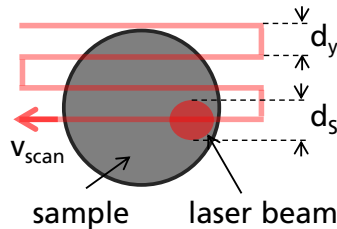

Figure 1: Schematic diagram of the laser treatment strategy (resulting process parameters: laser output power P_L, beam diameter d_S, hatch spacing d_y, scanning velocity v_{scan})

The peak temperature of the laser-induced temperature-time-profile is increased by increasing the laser output power starting at 50 W. In order to identify laser process parameters leading to a drying state similar to the state of a furnace-dried coating an iterative strategy consisting of systematical adaption of the process parameters and analysis of the laser-treated coatings is pursued (Figure 2).
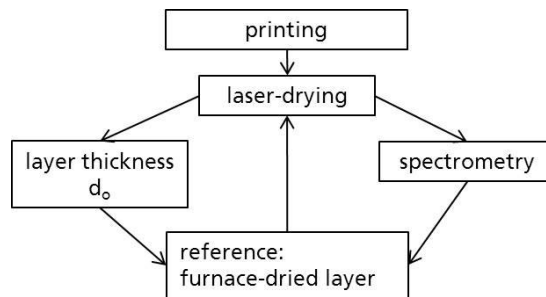

Figure 2: Experimental approach

The peak-temperature is not accessible by experimental measurements. Because of that FEM-

simulations (Finite Element Method) of the laser-induced temperature-time-profiles are carried out based on a heat-conduction-model of the coated steel substrate. For this purpose the optical properties of the printed thin film need to be determined in order to develop an adequate model of the laser-induced heat sources (Figure 3).
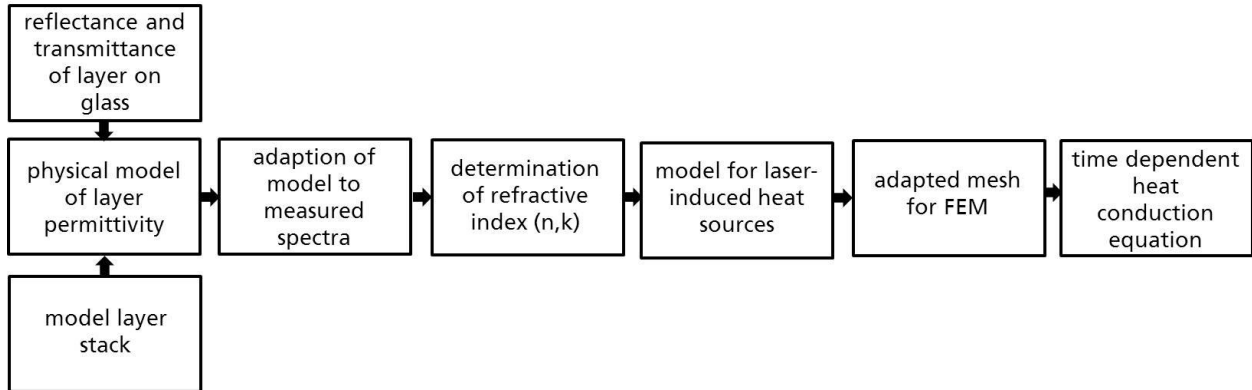

Figure 3: Schematic diagram of the model-based approach to simulate the laser-induced temperature-time-profiles

Keeping the scanning-velocity v_{scan} and the hatch spacing d_y constant, FEM-simulations with different values of the laser output power lead to a fundamental understanding of the correlation between the laser output power and the laser-induced temperature-time-profile. This model-based approach offers the possibility to investigate the coating properties as a function of the peak-temperature. The evolution of the layer thickness and the amount of uncondensed organic precursors is investigated by Fourier Transform Infrared Spectroscopy measurements (FTIR), UVVISNIR spectrometry and White Light Interferometry (WIM) as a function of the simulated peak-temperature. Finally, a furnace-dried thin film serves as a reference to obtain the optimal laser process parameters. The key issue of the presented investigation is, whether the laser-based drying-process allows for the same degree of network formation and solvent removal as the time-consuming furnace-process. Nanonindentation measurements are carried out on both furnace-dried and laser-dried multilayer systems with a coating thickness of ≈ 400 nm in order to investigate the Young's Modulus and Vickers hardness as a function of the type of the applied heat treatment. Within the laser-dried multilayer-system the laser-drying parameters are adjusted for every layer referring to the absorbance determined by UVVISNIR spectrometry in order to make sure that every layer is dried at the same temperature.

Results

A laser treatment with a simulated peak temperature of approximately $T_{max} \approx 400$ °C leads to a significant decrease of the FTIR-peaks associated with the organic ingredients (wave number 1500 - 1600 cm^{-1}) (Figure 4). At the same time the coating thickness is significantly reduced to (70 ± 15) nm. Further increase of the peak temperature to up to 700 °C does not have a significant effect on the amount of contained organic ingredients. On the contrary, the layer thickness is further decreased by increasing the peak temperature to ≥ 400 °C (Figure 4).
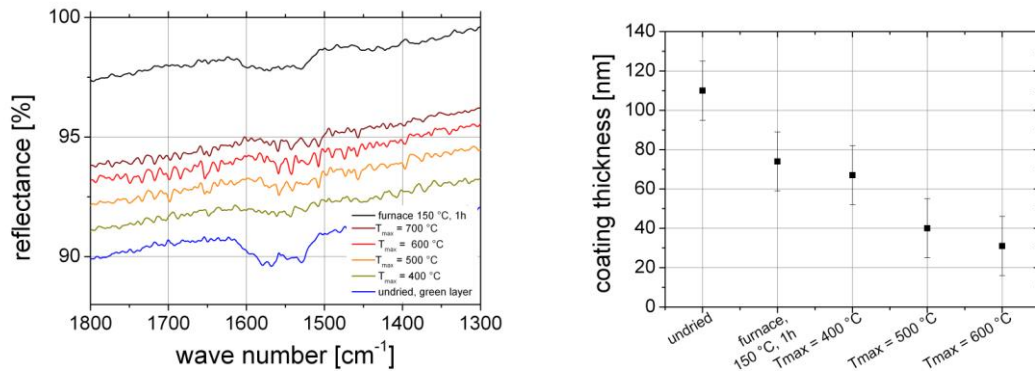
Figure 4: FTIR-spectra of laser treated layer (left) and the evolution of the layer thickness (right) as a function of the simulated peak temperature of the laser-induced temperature-time-profile (The vertical sequence of the spectra corresponds to the arrangement of the legend labels)

Referring to the FTIR-spectra and the coating thickness a drying-state comparable to furnace-dried films is successfully achieved byr a laser treatment with a simulated peak temperature of 400 °C (P = 50 W, v_{scan} = 2000 mm/s, d_y = 0,06 mm). The Vickers hardness and Young's Modulus of both a laser-dried and a furnace-dried multilayer-system (thickness 400 nm, number of layers 8 and 7 respectively) are summarized in table 1.

Table 1: Results of the nanoindentation measurements carried out on both a laser-dried and a furnace-dried multilayer system (test parameters: max. test load 0.1 mN, load time 20 s, hold time 30 s, Vickers Indenter)

drying process	Vickers hardness [HV]	Young's Modulus [GPa]	Indentation depth [nm]
laser	115 ± 20	21 ± 3	42 ± 4
furnace	160 ± 20	25 ± 3	35 ± 2

The higher hardness of the furnace-dried coating indicates a further advanced network formation which is due to the longer duration of the drying process (furnace: 1h, laser: 1 ms). The effect of this difference on the final coating properties achieved after the laser-based functionalization at significantly higher temperatures > 1200 °C will be investigated in further studies.

Acknowledgements

References

[1] Hawelka, D.; Stollenwerk, J.; Pirch, N.; Wissenbach, K.: Laser based production of thin wear protection films. Proceedings of the Laser Microfabrication Conference, ICALEO 2010, Anaheim, CA: LIA, Laser Institute of America, 2010, Paper 1709, 6 S.
[2] Hawelka, D., Stollenwerk, J., Pirch, N., Büsing, L., Wissenbach, K.: Laser based inline production of wear protection coating on temperature sensitive substrates. Phys. Proced. 12, Part A, 490-498, 2011

Electrophoretic deposition of nano-ceramics for the photo-generated cathodic corrosion protection of steel substrates

Ji Hoon Park[*], Kyoo Young Kim and Jong Myung Park

Graduate Institute of Ferrous Technology
Pohang University of Science and Technology (POSTECH)
San 31, Hyoja-Dong, Pohang, 790-784, Korea

[*] Presenter : jihun@postech.ac.kr

Corrosion is a destructive result of chemical reaction between a metal or metal alloy and its environment. Protective coatings are frequently employed in order to protect the steel from the corrosion. Among these, zinc coatings are most widely employed because of their good barrier property and sacrificial anodic performance. However, lifetime of the zinc coatings for the corrosion protection is limited. To overcome the drawback, inorganic TiO_2 coating has been extensively studied because it is electrochemically stable and it can be utilized as a photo-generated non-sacrificial anode [1, 2]. Under the ultraviolet (UV) illumination, TiO_2 can generate photo-electrons and then the generated electrons can inject to the metal via the conduction band. As a result, the open circuit potential of the metal can be shifted toward more negative potentials than the corrosion potential of the metal itself. Despite of its fascinating performance, pure TiO_2 coating suffers from the facile charge recombination reaction and, moreover, it cannot function photo-actively in the dark condition. Combination of other materials, which could separate the photo-electron from the TiO_2 and then store the electrons, will be the most promising way to overcome the drawbacks of pure TiO_2 coating. Tatsuma et al. demonstrated that WO_3 can store photo-electrons and subsequently release the photo-electrons in dark condition [3,4]. Many different materials are also demonstrated as electron storing materials, such as SnO_2 [5], Cu_2O [6] and MoO_3 [7]. In this study, WO_3 was employed because it is mostly well-known photo-electron storing materials. In addition, electrophoretic deposition (EPD) was utilized to deposit TiO_2-WO_3 nanoparticle on the stainless steel substrate (SUS 304). Electrophoretic deposition is achieved by coagulation of charged particles in a liquid suspension under an applied electric field. Recently, EPD has been intensively employed to fabricate the nano-structured functional ceramics composite layer because of its fascinating advantages such as versatility for application, cost effectiveness and simplicity. Especially, the uniform nano-structured packing ceramic film can be easily formed on steel substrate by electrophoretic deposition. In this study, TiO_2 (Degussa P25, particle size 25 nm, anatase and rutile mixture of 8:2) and WO_3 (particle size 90 nm) were used for the electrophoretic deposition. TiO_2 and WO_3 particle were dispersed in isopropyl alcohol (IPA) together with a particle charging additive (0.05M phosphoric acid di-butyl ester). The solutions of different particle concentration were prepared: TW 0 (TiO_2 30 $g \cdot L^{-1}$ + WO_3 0 $g \cdot L^{-1}$), TW 20 (TiO_2 24 $g \cdot L^{-1}$ + WO_3 6 $g \cdot L^{-1}$) , TW 40 (TiO_2 18 $g \cdot L^{-1}$ + WO_3 12 $g \cdot L^{-1}$) , TW 60 (TiO_2 12 $g \cdot L^{-1}$ + WO_3 18 $g \cdot L^{-1}$) . The prepared suspensions were ultrasonicated for 1 hour to obtain a homogeneous dispersion of nano particles. The electrophoretic deposition (EPD) was performed at constant voltages of 30 V for 1 min. The distance between the substrates and counter electrodes was 15 mm. Then, the deposited specimen was dried at 60 °C in convection drying oven. The surface

morphology was observed using scanning electron microscopy (SEM, Hitachi SU-6600). Before SEM observations, the samples were coated with 10 nm of Pt/Pd. Furthermore, in order to investigate the cathodic protection ability of EPD coating layers, free corrosion potential (E_{corr}) measurements were carried out under the UV irradiation with a Gamry Reference 600 with PCI4 Controller. 200W mercury-xenon lamp was employed as an ultraviolet (UV) light source. The optical properties of the electrodes were also characterized with a UV−vis diffuse reflectance spectrophotometer (Shimadzu UV2450). The X-ray diffractometer (XRD, D8 Advance, Bruker AXS) analysis using CuKa radiation was conducted to determine the actual ratio of deposited concentration of each type of ceramic particles on 304 stainless steel. Figure 1 shows SEM micrograph of the electrophoretically deposited layers on 304 stainless steel from the suspension of pure TiO_2 (TW 0) and TiO_2-WO_3 hybrid solution with the different concentrations of 20 % WO_3 (TW 20), 40 % WO_3 (TW 40) and 60 % WO_3 (TW 60) of total weight of particles. As shown in SEM micrograph, TiO_2 and WO_3 nanoparticles were successfully deposited by electrophoretic motion of charged particle under the constant applied voltage. There was no noticeable homo-aggregation of the same kind of particle in the co-deposited layer. In other words, TiO_2 and WO_3 particle were homogeneously blended and uniformly deposited on the stainless steel substrate. The film thickness of each layer was around 10 μm. In addition, X-ray diffractometer (XRD) analysis was performed to confirm the WO_3 concentration in the electrophoretically deposited layer. Figure 2 shows the variation of the XRD patterns of the deposited layer on the stainless steel from the different WO_3 concentrations of suspension. From XRD pattern, it can be demonstrated that the particle concentrations of WO_3 in the deposited layers on the stainless steel are proportional to the WO_3 concentrations of   the suspensions.
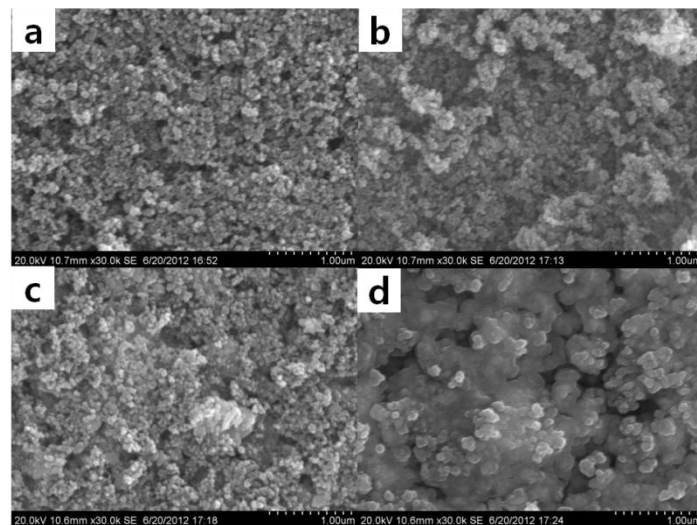

Figure 1. SEM micrograph of electrophoretic deposited layers on 304 STS with TW 0 (pure TiO_2) (a) and TiO_2-WO_3 hybrid layer with different particle concentrations of   TW 20 (20 % WO_3) (b), TW 40 (40 % WO_3) (c) and TW 60 (60 % WO_3)   (d) of total weight of particles.

The optical absorption spectra of the electrophoretically deposited layers with different WO_3 concentrations are shown in Figure 3 (a). The spectra for these samples have similar shapes with absorption peak in the range of 300 to 400 nm, which is due to the charge transfer process from valence band to conduction band in TiO_2 particles (anatage 3.2 eV & rutile 3.02 eV). However, the absorption edges of the deposited layers with different WO_3 concentration are a little bit different (Figure 3(b)). Compared with the TW 0 (pure TiO_2), WO_3 co-deposited samples possessed lower optical absorption edges. The higher WO_3 concentration, the more obvious the red shift of the sample is. For determining energy band gaps, the graph of optical absorption edge $(ahv)^{1/2}$ versus energy of photo (hv) was plotted as given in Figure 3 (b). The estimated band gap was decreased with

increasing WO_3 concentration. The reduction of band gap energy of co-deposited sample would be originated by the hybridization of smaller WO_3 band gap (2.8 eV).
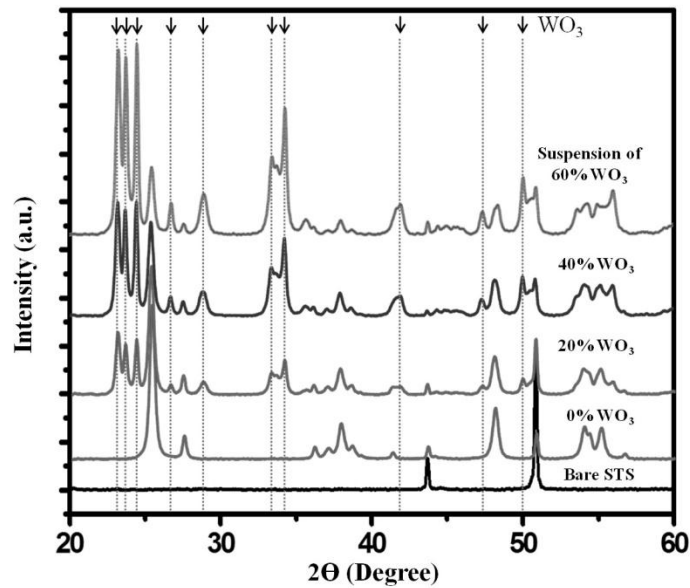

Figure 2. The variation of XRD patterns of electrophoretically deposited layers on 304 stainless steel with different WO_3 concentrations in the suspensions.
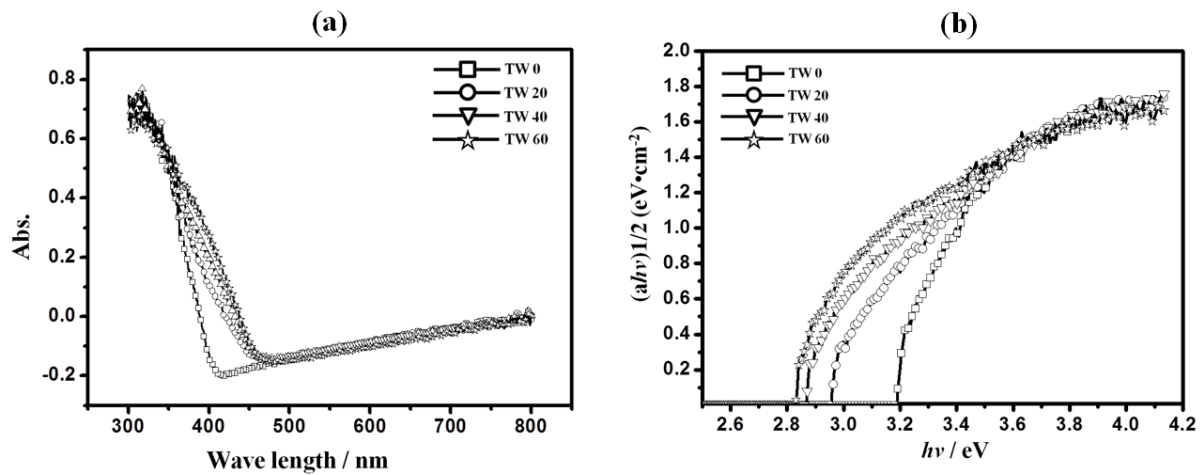

Figure 3. (a) The optical absorption spectra and (b) the optical absorption edge (ahv)$^{1/2}$ versus energy of photon (hv) of electrophoretically deposited layer on the stainless steel with different WO_3 concentrations.

Figure 4 shows the open circuit potential changes of electrophoretically deposited TiO_2-WO_3 layer on the stainless steel in 3.5 wt. % NaCl solution upon UV light on-off. Under the UV irradiation, the open circuit potential of the electrophoretically deposited stainless steel immediately dropped down in the range of - 0.5 V_{SCE} and -0.7 V_{SCE}. However, the increase of the WO_3 concentration caused the slowdown of the rate of potential drop. The free corrosion potential of bare 304 stainless steel was about -0.1 V_{SCE}. Thus it is assumed that, under the ultraviolet (UV) illumination, the deposited layer would generate photo-electrons and then the generated electrons would be injected to the metal via the conduction band. Therefore, the open circuit potential of the electrodeposited stainless steel was shifted to more negative values than its own corrosion potential. Obviously, all deposited layers with different ratios of TiO_2/WO_3 provided a cathodic protection ability to the stainless steel. However, soon after light

was turned off, the open circuit potential recovered to the original value (the free corrosion potential of stainless steel). The higher the WO_3 concentration in the deposited layer, the more delayed the time of potential recovery was. Namely, it was due to the electron storage ability of WO_3. Tatsuma et al. demonstrated that WO_3 can store photo-electrons under light and subsequently release the photo-electrons in dark condition. The longer recovery time of potential means the longer corrosion protection of 304 stainless steel in dark condition. In the case of TW 60 sample, the open circuit potential of electrophoretically deposited 304 stainless steel maintained below the corrosion potential of the stainless steel substrate for 5 hours.
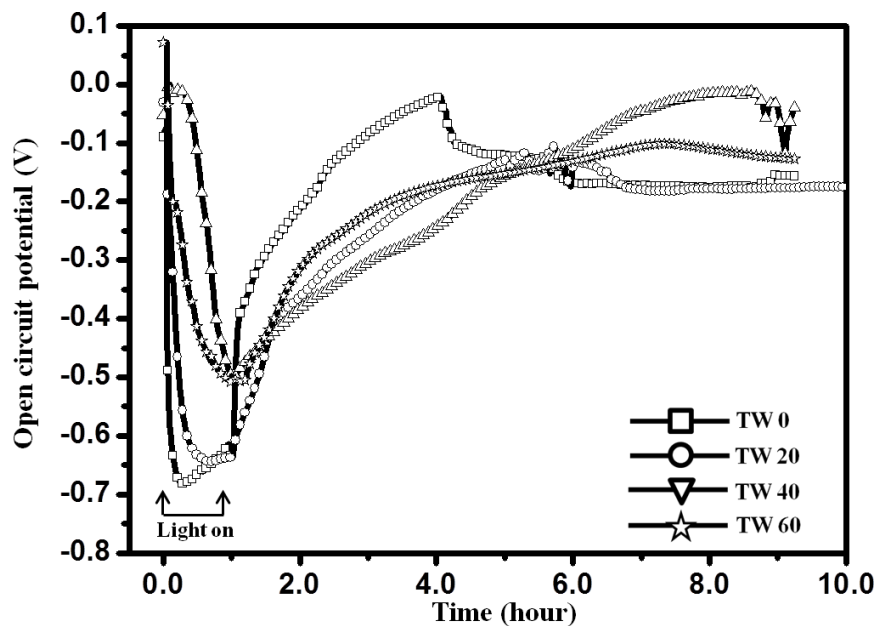

Figure 4 Effect of WO_3 concentration of EPD layer on the changes of open circuit potential of TiO_2-WO_3 particle deposited 304 STS in the 3.5 wt.% NaCl solution under UV irradiation.

In conclusion, in this study, TiO_2-WO_3 hybrid layer successfully deposited on 304 STS via an electrophoretic deposition method in the applied voltage of 30V for 1 min. The TiO_2-WO_3 co-deposited layer was stable in the aqueous NaCl solution. Moreover, it was demonstrated that TiO_2-WO_3 electrodeposited layer can protect the 304 stainless steel both under UV irradiation and in dark (light off) condition. The increase of WO3 content in the deposited layer brought about the delay of potential recovery time in dark condition.

[1] J. Yuan and S. Tsujikawa, J. Electrochem. Soc., 142, 3444 (1995).
[2] T. Imokawa, R. Fujisawa, A. Suda and S. Tsujikawa, Zairyo-to Kankyo, 43, 482 (1994)
[3] T. Tatsuma, S. Saitoh, Y. Ohko, A. Fujishima, Chem. Mater., 13, 2830 (2001)
[4] T. Tatsuma, S. Saitoh, P. Nhaotrakanwiwat, Y. Ohko, A. Fujishima, Langmuir, 18, 7777 (2002)
[5] R. Subasri, T. Shinohara, Electrochem. Commun., 5, 897 (2003)
[6] J.P. Yasomanee, J. Bandara, Sol. Energy Mater. Sol. Cells, 92, 348 (2008)
[7] Y. Takahashi, P. Ngaotrakanwiwat, T. Tatsuma, Electrochim. Acta, 49, 2025 (2004)

Photocatalytic sol-gel TiO_2 coatings on steel substrate: effect of surface treatment of coated steel substrate on the photo-catalytic activity

Woo Sung Kim[*], Ji Hoon Park, Kyoo Young Kim and Jong Myung Park

Graduate Institute of Ferrous Technology
Pohang University of Science and Technology (POSTECH)
San 31, Hyoja-Dong, Pohang, 790-784, Korea

[*] Presenter : docgotak@postech.ac.kr

There has been much effort to utilize the solar energy in a chemical reaction because the so-called photocatalysis is very economic and environmentally friendly technique. A photocatalyst is the material capable of utilizing sunlight to convert the gaseous materials, decompose the pollutants and split water to produce hydrogen. TiO_2 has been most widely used due to its low cost, high stability and most efficient photoactivity. TiO_2 photocatalyst can be applied on the various substrates such as glass, quartz, tile, stainless steel and paper [1-3]. However, galvanized steel (GI) has been rarely studied as a substrate for immobilizing a photocatalyst. GI has many advantages such as good mechanical property, high anticorrosion performance and good material reliability. In this study, GI was employed for the substrate of TiO_2 photocatalyst. In addition, the sol-gel method was used in order to immobilize TiO_2 layers on the substrate. The crystalline TiO_2 powder (Degussa P-25) was incorporated into a precursor sol in order to enhance the photocatalytic activity of TiO_2 films. Nevertheless, TiO_2 has a wide bandgap of 3.2 eV, so it can only absorb the UV portion of the solar spectrum [4]. To utilize a larger fraction of the solar spectrum, TiO_2 should be modified to make the bandgap smaller. Recently, it has been reported that TiO_2 mixed with rare earth elements, such as La, Nd, Eu and Ce, showed photoactivity in the visible light [5-7]. Among them, Ce showed the best activity in visible region consistently when mixed with TiO_2 [8, 9]. For that reason, cerium oxide layer was deposited on GI surface as an interfacial layer of TiO_2 photocatalytic film. In the study, the effect of cerium conversion coatings on the photocatalytic activity of TiO_2 layer was mainly discussed. The effect of incorporation of commercial crystalline TiO_2 particle (P-25) into TiO_2 sol-gel layer was also evaluated.

Cerium oxide interfacial layer was formed by applying the cerium conversion coating on galvanized steel. The ingredient of the solution and specific formation method for the cerium conversion coating are shown in Table 1. In order to prepare the photocatalytically active galvanized steel, All chemicals to prepare TiO_2 powder modified sol (PMS) were used as received, which include titanium iso-propoxide (TTIP, Aldrich, 97%), iso-propanol (IPA, Sam Chun Chemical, 99.8%) polyethylene glycol (PEG, Aldrich, MW:300), de-ionized water,

nitric acid (60%) and P-25 powder. The precursor solution consisted of 70 g TTIP, 50g IPA and 9g PEG. The solution was stirred at room temperature for approximately 1 hour. Then the pre-mixed solution containing 30g IPA, 2g nitric acid and 4 g of de-ionized water was added drop-wise under vigorous stirring. Subsequently, P-25 powder was incorporated into a precursor sol solution. The loading concentrations of P-25 powder were 0, 10, 20, 40 and 80 $g \cdot L^{-1}$. After aging the solution at room temperature for 1 day, the pre-cleaned galvanized steel substrates were coated with P-25 powder modified TiO_2 sol-gel solution using a dip-coater. The dipping time was 5 minutes and the withdrawing speed of the sample was $2m \cdot min^{-1}$. The dip-coated specimens were dried at 65 ^{o}C for 1 hour and then calcined at 300 ^{o}C for 2 hour.

Solution			Dipping time at RT (min)	Drying Time at RT (hr)
$Ce(NO_3)_3 \cdot 6H_2O$ (mM)	pH	H_2O_2 (g/L)		
10	3.8	30	30	12

Table 1. Formation method for the cerium oxide interfacial layer.

The surface morphologies of the sample were observed by a scanning electron microscopy (SEM, Hitachi SU-6600). Figure 1 shows SEM surface morphology of specimens with the different loading concentration of P-25 powder. As increasing the loading concentration, the agglomerated TiO_2 particle was clearly appeared on the surface of the sol-gel film. Many cracks were observed in all substrates. The crack formation of TiO_2 films could not be avoided because of the internal stress increase and film volume shrinkage upon thermal treatment. The cracks were mainly formed at valley areas in rough surface of galvanized steel because of relatively thicker film in the areas. On the other hand, the incorporation of crystalline TiO_2 particle was helpful to form a crack-less film. It seems to be due to the stress relaxation in the interface between particle and film matrix. However, the high concentration of P-25 powder deteriorated the sol-gel film integrity and thus forming a crack again.
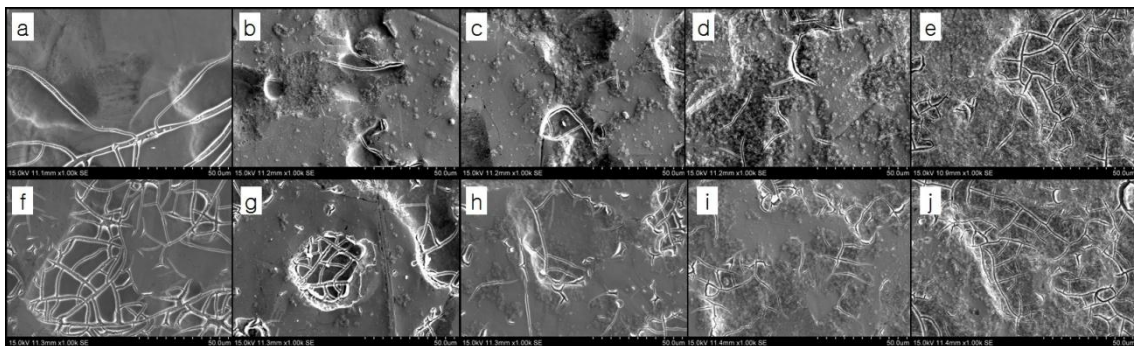

Figure 1. SEM microscopy of the surface of TiO_2 film made from (a) non CeCC(Cerium conversion coating)-PMSGM 0 $g \cdot L^{-1}$; (b) non CeCC-PMSGM 10 $g \cdot L^{-1}$; (c) non CeCC-PMSGM 20 $g \cdot L^{-1}$; (d) non CeCC-PMSGM 40 $g \cdot L^{-1}$; (e) non CeCC-PMSGM 80 $g \cdot L^{-1}$; (f) CeCC-PMSGM 0 $g \cdot L^{-1}$; (g) CeCC-PMSGM 10 $g \cdot L^{-1}$; (h) CeCC-PMSGM 20 $g \cdot L^{-1}$; (i) CeCC-PMSGM 40 $g \cdot L^{-1}$ and (j) CeCC-PMSGM 80 $g \cdot L^{-1}$

The optical absorption spectra of P-25 modified sol-gel film coated on bare-GI and cerium

conversion coated GI are shown in Figure 2. The spectrum shows an absorption onset at 380 nm for P-25 modified sol-gel layer. The higher the loading of P-25 particle, the higher the absorption of UV light (below 380 nm) is. Obviously, the photocatalytic film formed on the cerium conversion coated GI showed a red shift. CeO_2 is an n-type semiconductor whose bandgap is around 2.8 eV. Therefore, the cerium oxide layer would be responsible for the observed red shift about 50 nm. The coupled semiconductor (TiO_2-CeO_2) mechanism for the visible light activity was illustrated in Figure 3.
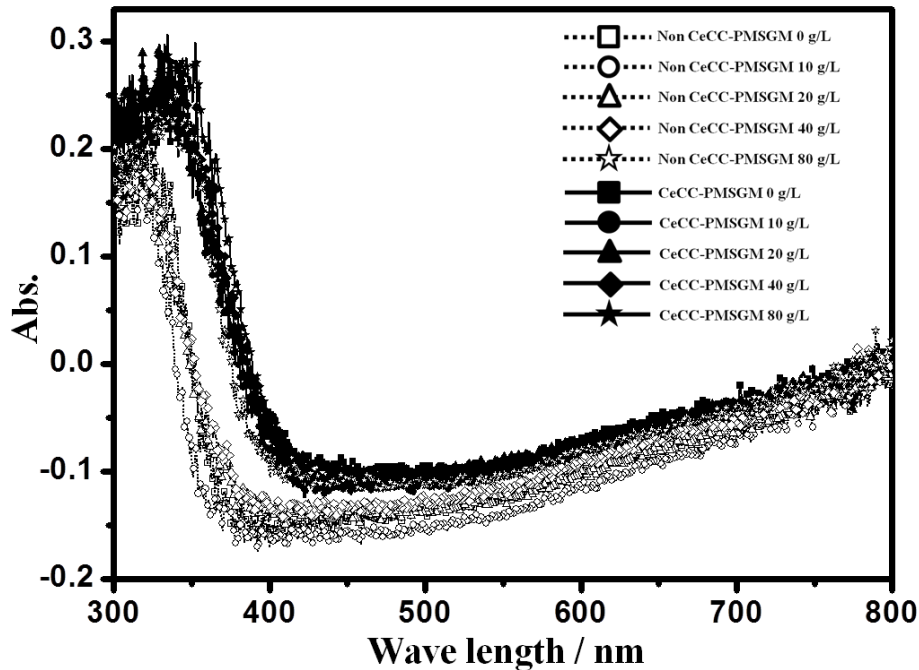

Figure 2. Optical absorption spectra of P-25 modified sol-gel TiO2 film coated on bare-GI (dotted lines) and cerium conversion coated GI (solid lines).
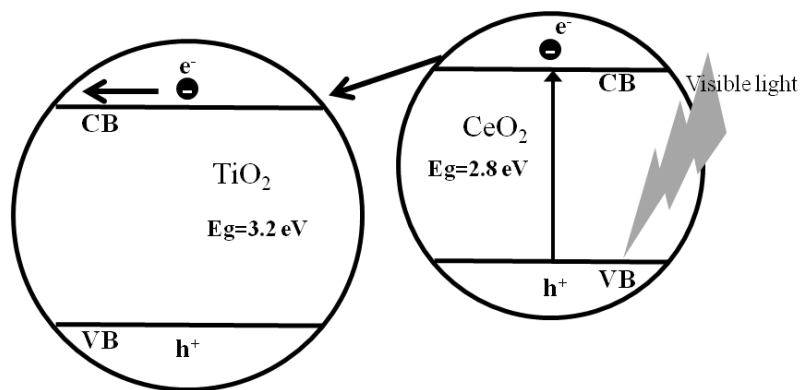

Figure 3. The coupled semiconductor (TiO_2-CeO_2) mechanism for the visible light activity.

The photocatalytic activity of the coated sample was evaluated by measuring the rate of photodegradation of methyl orange in aqueous solution. The photo-induced degradation of methyl orange was monitored in the presence of coated sample under the ultra-violet (UV) light source (200W mercury xenon lamp) for 4 hour. The photocatalytic activities of P-25 modified sol-gel film on GI with different particle loading concentration are shown in Figure 4. It can be demonstrated that the photocatalytic activity was enhanced with increasing P-25

particle loading concentration. Moreover, the existence of the cerium oxide interfacial layer formed GI sample provided better photocatalytic activity. The result is good agreement with the UV-visible light absorption behaviors of the sample. In other word, the enhancement in the photocatalytic activity may come from the hetero-junctions of TiO_2-CeO_2 in the coupled photocatalysts as explained in Figure 3. In conclusion, high P-25 powder loading of TiO_2 coating layer on GI in combination with the CeO_2 interfacial layer showed the best photocatalytic activity.
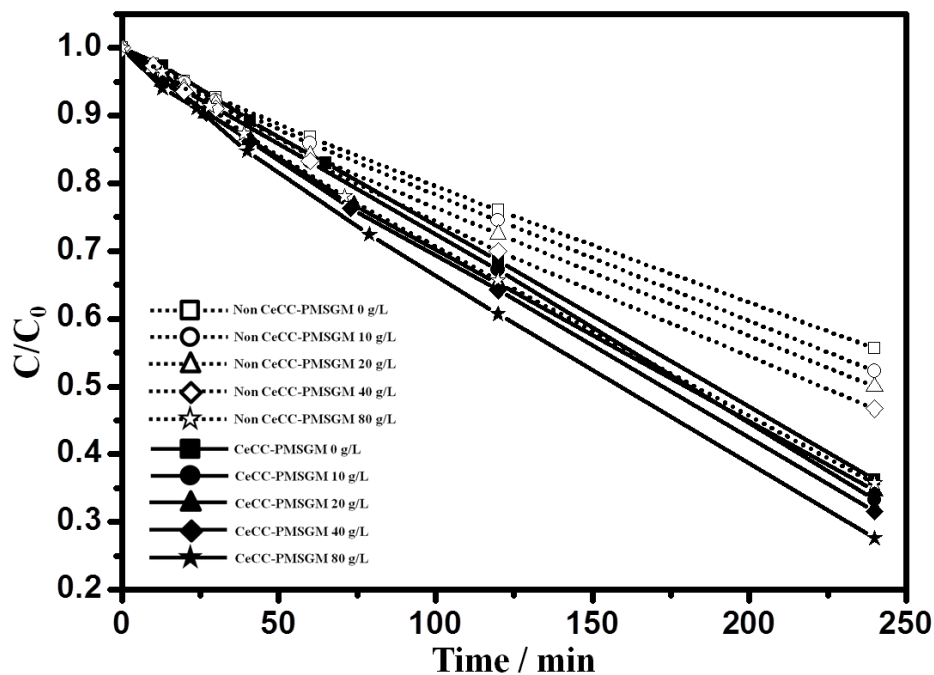

Figure 4. The degradation rate of methyl orange solution in UV light with P-25 modified sol-gel TiO_2 film coated on bare-GI (dotted lines) and cerium conversion coated GI (solid lines).

[1] J.C. Yu et al., Appl. Catal. B: Environ. 36 (2002) 31
[2] Y.F. Zhu et al., Appl. Surf. Sci. 158 (2000) 32.
[3] J.R. Bellobona et al., J. Photochem. Photobiol. A. 84 (1994) 83.
[4] Y. Xie et al., Catalysis Letters 118 3 231 (2007)
[5] Y. Xie et al., Appl. Surf. Sci., 221 (2004) 17
[6] H. Wei et al., J. Mater. Sci., 39 (2004) 1305
[7] F.B. Li et al., Chemosphere, 59 (2005) 787
[8] T. Tong et al., J. Coll. Interface Sci., 315 (2007) 382
[9] B. Liu et al., Surf. Sci., 595 (2005) 203

Nanofibrillated Cellulose (NFC) coat weight predictions when coating onto paper

Finley Richmond and Douglas W. Bousfield

Department of Chemical and Biological Engineering

The University of Maine

Orono, ME 04469-5737

Presented at the 16th International Coating Science and Technology Symposium,

September 9-12, 2012, Midtown Atlanta, GA[1]

Nanofibrillated cellulose (NFC) has the potential to be produced at low cost at paper mills through mechanical methods. NFC has been shown to create a layer with fine pores over paper fibers that can capture ink pigments, increasing the print density of the surface. However, NFC is produced at low solids. The rheology of NFC suspensions becomes complex as the solids are increased [1]. The method to coat moderate solids NFC onto paper is not clear in the literature.

Suspensions of NFC at different solids were coated onto paper surfaces with a forward roll coating system as depicted in Figure 1. NFC was produced as described earlier as well as the rheology of the NFC suspension was reported [1]. The NFC suspensions were filtered to change the solids level and to obtain the specific filtration cake resistance. Figure 2 shows that the filtration rate follows the standard behavior. Excess suspension was applied in front of the nip. The computer controlled rolls rotate one time at the speed of interest to apply the suspension to the paper. A commercial finite element package (COMSOL) using the Carreau model to describe the shear thinning nature of the suspension is used to predict the coat weight.

Figure 3 shows the pressure field predicted in the nip. The coat weight is calculated by integrating the velocity profile perpendicular to the flow direction at any location. The nip load is obtained by integrating the pressure pulse in the positive part of the curve. Coat weight predictions are shown in Figure 4.
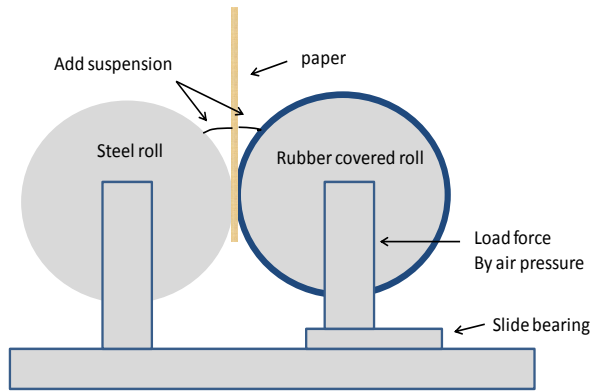

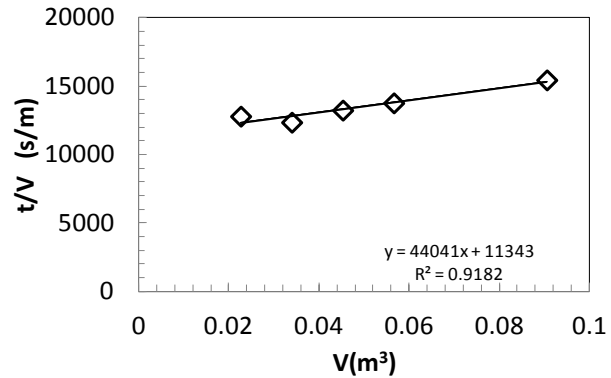Figure 1. Flooded size press configuration.

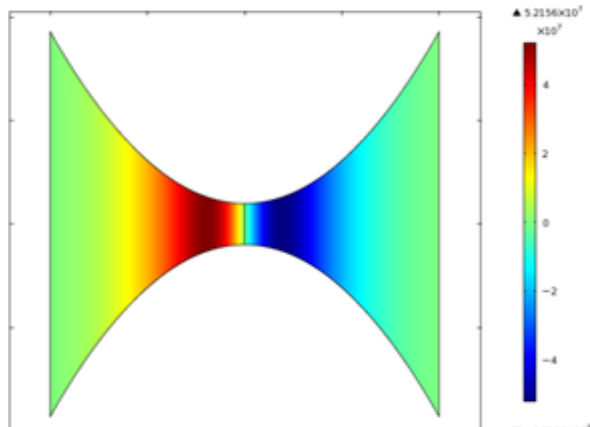Figure 2. Filtration time (t) and volume (V).
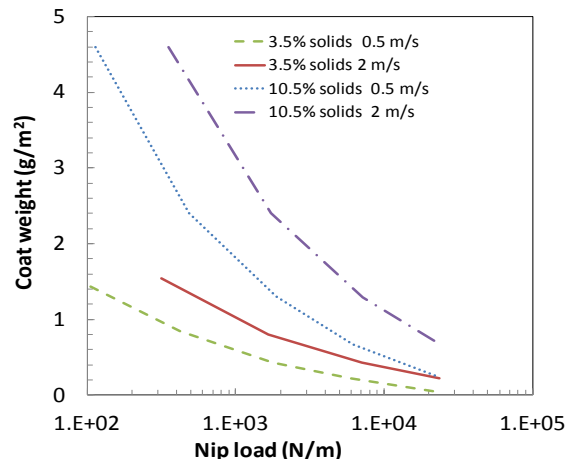

Figure 3. Pressure field predicted in nip.

Figure 4. Coat weight predictions for flooded case.

The coat weights obtained with the flooded nip conditions are shown in Figures 5 and 6. Three key unexpected results are clear:

1. The coat weight slowly decreases with increasing nip load, much different than predicted in Fig. 4,

2. The coat weight moderately increases with increasing solids, much less than predicted in Fig. 4,

3. And the coat weight is insensitive to speed.

In Fig 6, as the solids increase by a factor of three, the coat weight increases less than a factor of two.
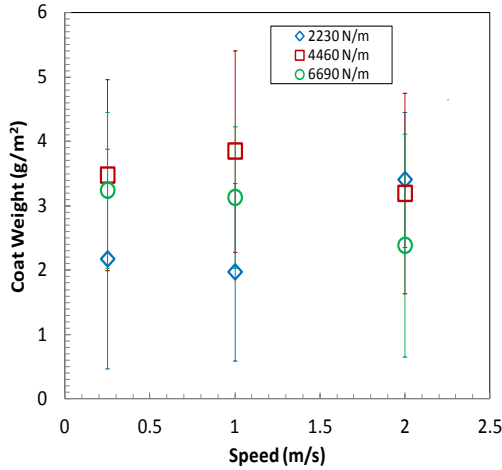

Figure 5. Coat weight measured at different speeds for 3% solids suspension. Error bars are standard deviation from five repeats.
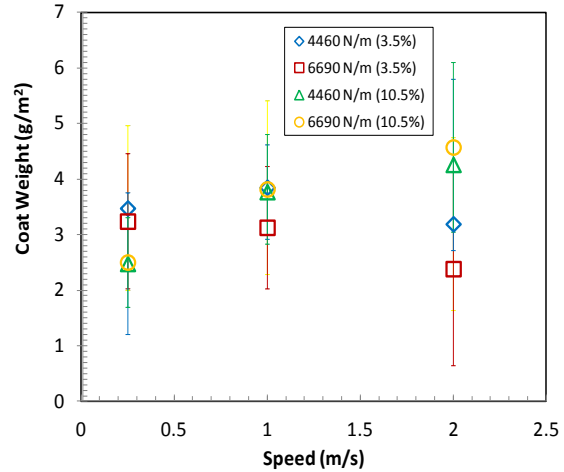
Figure 6. Coat weight measured at different speeds for 3% and 10.5% solids suspension at two loads. Error bars are standard deviation from five repeats.

The results indicate that the coat weight is determined by two separate mechanisms. At low speeds, water is forced into the paper substrate, forming a filtercake of NFC on the paper surface. This material increases the amount of NFC that is able to pass through the nip. This filtration event seems to dominate at low speeds because there is more time for dewatering in the nip. At high speeds, the coat weight is determined by the hydrodynamic forces generated in the nip. This is the amount of NFC that passes in the fluid phase through the nip.

The amount of time for filtration can be estimated by the length of the "puddle" in front of the nip divided by the nip length. The average filtration pressure is the nip loading divided also by this nip length. Therefore, with use of the standard filtration equations, using parameters to fit the results in Fig. 2, the amount of material that would be deposited on the web can be predicted. This is similar to the method used by Devisetti and Bousfield to predict penetration in the nip for a pure fluid [2]. As the nip speed increases, there is less time for dewatering. As nip pressure increases, more dewatering is predicted. By looking at the coat weight

predictions from the fluid flow through the nip compared to the amount of dewatering, the trends of the experimental results make sense. The lack of sensitivity to speed comes from large dewatering at slow speeds that would deposit more NFC on the paper web but at high speeds, large hydrodynamic forces would generate a more open gap allowing more NFC onto the paper. As nip load increases, the gap should decrease to generate less coat weight, but these loads would increase the dewatering mechanism.

By a simple addition of the coat weight predicted by fluid flow, as in figure 4, to the amount of dewatering predicted by the standard filtration equations, a method to predict coat weight is obtained. In reality, a number of other factors can be at play and the dewatering mechanism would interact with the fluid flow calculation through a mass balance. For most cases, the predicted results are less than the measured results, but they are in the same order of magnitude.

Concluding Remarks

NFC is able to be coated onto paper with metered and flooded size press methods up to solids levels of 10%. The coat weights are insensitive to speed and moderately sensitive to nip loading and solids. The results can be explained by two different mechanisms. At low speeds, the dewatering in the nip gives rise to a filtercake of material on the paper web. At high speeds, the hydrodynamic forces balance the nip loading to control the coat weight. A model is presented that predicts the general trends and the correct range of values.

1. Finley Richmond, Albert. Co, and Douglas. W. Bousfield, "The coating of nanofibrillated cellulose onto paper using metered and flooded size press methods"., Proc. Technical Association of Pulp and Paper, PAPERCON, 2012.
2. Devisetti S.K. and D. W. Bousfield, "Fluid absorption during forward roll coating of porous webs", Chem. Eng. Sci., (2010) 65: 3528-3537.

Laser- Drawn Features on Nanoparticle Films

Sanjeev Kumar Kandpal (*), Kody Allcroft (*), Michael D. Mason (*),

Douglas W. Bousfield (*), David J. Neivandt (*)

(*) Department of Chemical and Biological Engineering

The University of Maine, Orono, Maine -04473

Presented at the 16th International Coating Science and Technology Symposium,

September 9-12, 2012, Midtown Atlanta, GA[1]

Introduction:

The present work explores the silver (Ag) nanoparticles film-Laser interaction based applications in the field of printed electronics, sensors, anti-counterfeiting, optical grating. Ag having the highest conductivity among metals makes it most sought after material for providing conductivity in electronics and even its oxide form is also conductive. Ag in nanoparticle size range show interesting optical, physical and electronic properties like melting point depression (Buffat & Borel, 1976), large absorption and scattering cross section when compared to bulk silver, have a color that depends upon the size and the shape of the particle, high surface to volume ratio, tunable surface Plasmon resonance (SPR) peak wavelength, metal enhanced fluorescence (MEF) (Geddes *et al.*, 2003), surface enhanced Raman scattering (SERM) (Li & Peng, 2010) antibacterial application, diagnostic application, enhanced thermal and conductivity application. In the present work we fabricated three dimensional features on Ag nanoparticles film using laser, these structure showed interesting fluorescent properties. We are also looking into fabricating structure on polymer-Ag nanoparticles films and characterize them for the conductivity, optical, fluorescence properties. These structures might serve as conductive path on polymer-nanoparticle film, paving way for alternative way of fabricating printed circuits.

---

2. Materials and Methods:

2.1. Synthesis:

Silver nanospheres were made using single-pot redox chemical techniques according to published material (Turkevich et al., 1951; Pillai and Kamat, 2004). In this we make use of a soluble metal salt (silver nitrate), a reducing agent (sodium citrate) and a stabilizing agent (excess sodium citrate). Synthesis starts with nucleation step, followed by nanoparticle growth and the stabilizing agent caps the particle leaving a negatively charged surface helping to avoid aggregation (Rivas *et al*., 2001). We start with cleaning all the glass wears with concentrated nitric acid, 600mg of sodium citrate dissolved in 160 ml of 18MΩ pure water in a 500 ml round bottom flask. This was then brought to a temperature of 95°C in an oil immersion bath. Simultaneously, 40mg of silver nitrate was dissolved in 40 ml of 18MΩ ultrapure water in a glass beaker. This was then added to the round bottom flask containing sodium citrate solution and heated to the same temperature (95°C) under constant stirring. The temperature was maintained until the reaction was complete, usually less than 1 h. The heating, stirring is stopped and solution is allowed to cool to room temperature. To impart electrostatic stability to nanoparticles, excess of stabilizing agent was added. The size of the nanoparticles is measured using Dynamic light scattering technique (Malvern, Zetasizer Nano-ZS) and also using Transmission electron microscope and UV-Vis Spectroscopy. Fig. 1A shows a transmission electron micrograph (TEM) image of the as-prepared silver nanoparticles prior to use. From the image data the average diameter was estimated to be approximately 100 nm.

2.2. Nanoparticles Film Making

Nanoparticles solution synthesized using above described method is very dilute in nature. To increase the number density of particles, the solution was subjected to rotation vaporization using Rotary Evaporator (Rotovap) instrument (BUCHI Rotavapour R-205). The solution was concentrated from 0.013wt% to 0.102wt%; the solution was then characterized using DLS and UV-Vis spectroscopy. 100μl of this solution was drop casted on 22x22mm cover slip and allowed it to air dry.

2.3. Exposing film to laser and characterization them:

The drop casted film was then subjected to 532nm continuous wave laser, the film was scanned under laser in raster pattern using an x-y scanning stage and the scan stage was controlled using LabVIEW software. Laser exposed films were characterized using optical microscope, CLSM (Confocal Laser Scanning Microscope), SEM (Scanning Electron Microscope), AFM (Atomic Force Microscope), XRD (X-ray Diffraction), EDAX (Energy-dispersive X-ray spectroscopy).

3. Results
3.1. Characterization of particles:

Nanoparticle solution was characterized using DLS, UV-Vis spectroscopy and TEM.

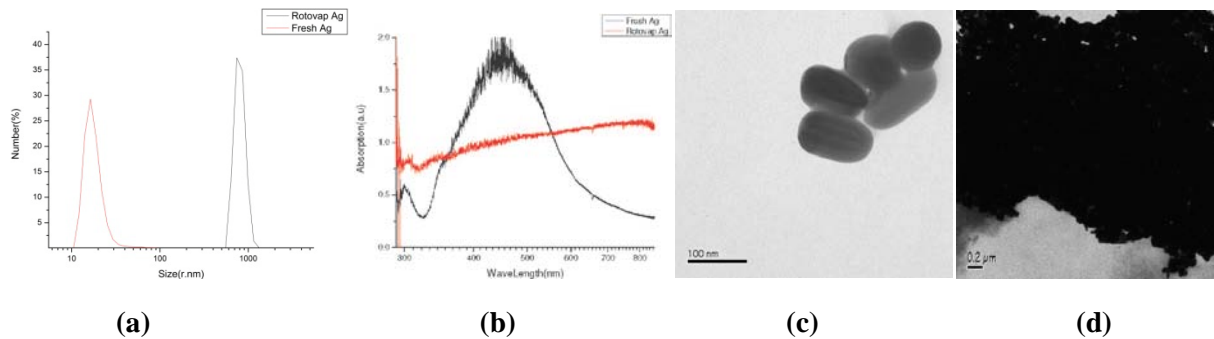(a)   (b)   (c)   (d)

Figure1: DLS (a), UV-Vis spectrum (b), TEM image of freshly made silver (c), TEM image of Rotovap concentrated silver.

The DLS graph shows that the freshly made Ag particles are around 50nm in radius and rotovap concenrated are around a micron. Theses numbers are complemented by TEM images and they also tel us about the shape of the particles. In UV-Vis graph the flat red cuve shows the aggregation effect of particles and black curve is the typical UV-Vis curve of 100nm Ag particles.
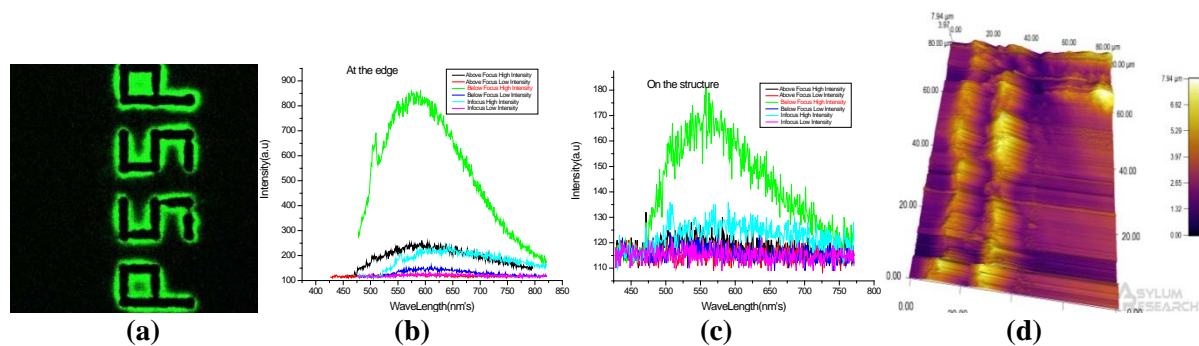

(a)   (b)   (c)   (d)

Figure2: Confocal Image (a), Fluorescence spectrum at the edge of the laser drawn structure (b), on the surface of laser drawn structure (c), AFM of letter 'P' (d).

Confocal imaging (Figure2 (a)) of the laser drawn structure showed strong fluorescence emission from the edges of the structures. The emission was quantified by measuring the fluorescence spectrum of the signal and was compared with signal from the edges (Figure2 (b)) to signal from the surface of the structure (Figure2 (c)). The fluorescence spectrum also shows that the emission is coming from below the structure at the edges (different curves in the spectrum represents different level along the z-axis of the structure) and the broad emission wavelength range. This fluorescent nature of the structures shows there potential in Anti-Counterfeiting application, effective marketing techniques for products.AFM image (Figure2 (d)) of tail of letter 'P' quantified that the structures have 3rd dimension (~8μm) also.

4. Conclusion

1. Successfully able to draw 8μm size feature on silver nanoparticle film.

2. Laser drawn structures were fluorescent at the edges.

5. References

- Buffat, P.H, and Borel, J-P. 1976. Size effect on the melting temperature of gold particles. Physical review A, 13(6), 2287–2298.
- Geddes, C. D, Haishi. C, Gryczynski. I, Gryczynski. Z, Fang. J, and Lakowicz. J.R, "Applications of Indocyanine Green to in Vivo Imaging †" *J. Phys. Chem. A (*2003), 107, 3443-3449.
- Li, W, Yanyan Guo, and Peng Zhang. "SERS-Active Silver Nanoparticles Prepared by a Simple and Green Method." *The Journal of Physical Chemistry C* 114, no. 14 (2010): 6413-6417.
- Turkevich. J, Stevenson. C, and Hillier. J "A Study of nucleation and growth processes." *Discussions of the Faraday Society* 11 (1951): 55-75.
- Rivas, L, Sanchez-Cortes, S, and Garcia-Ramos, J.V,. "Growth of silver colloidal particles obtained by citrate reduction to increase the Raman enhancement factor." *Langmuir* 17, no. 3 (2001): 574-577.
- Pillai, Z, S. "What factors control the size and shape of silver nanoparticles in the citrate ion reduction method" *The Journal of Physical Chemistry B* 3, no. 10 (2004): 945-951.